Applied and Environmental Microbiology, Sept. 2009, p. 5586–5591 Vol. 75, No. 17
0099-2240/09/$08.00+0 doi:10.1128/AEM.00490-09

Extracellular Iron Biomineralization by Photoautotrophic Iron-Oxidizing Bacteria▽†

Jennyfer Miot,[1]* Karim Benzerara,[1] Martin Obst,[2,3] Andreas Kappler,[3] Florian Hegler,[3] Sebastian Schädler,[3] Camille Bouchez,[1] François Guyot,[1] and Guillaume Morin[1]

Institut de Minéralogie et de Physique des Milieux Condensés, UMR 7590, CNRS, Universités Paris 6 et Paris 7, Paris, and IMPMC, 140 Rue de Lourmel, Paris, France[1]; BIMR, McMaster University, Hamilton, and Canadian Light Source, 101 Perimeter Road, Saskatoon, Saskatchewan, Canada[2]; and Geomicrobiology, Center for Applied Geoscience, University of Tuebingen, Sigwartstrasse 10, 72076 Tuebingen, Germany[3]

Received 27 February 2009/Accepted 6 July 2009

Iron oxidation at neutral pH by the phototrophic anaerobic iron-oxidizing bacterium *Rhodobacter* sp. strain SW2 leads to the formation of iron-rich minerals. These minerals consist mainly of nano-goethite (α-FeOOH), which precipitates exclusively outside cells, mostly on polymer fibers emerging from the cells. Scanning transmission X-ray microscopy analyses performed at the C K-edge suggest that these fibers are composed of a mixture of lipids and polysaccharides or of lipopolysaccharides. The iron and the organic carbon contents of these fibers are linearly correlated at the 25-nm scale, which in addition to their texture suggests that these fibers act as a template for mineral precipitation, followed by limited crystal growth. Moreover, we evidence a gradient of the iron oxidation state along the mineralized fibers at the submicrometer scale. Fe minerals on these fibers contain a higher proportion of Fe(III) at cell contact, and the proportion of Fe(II) increases at a distance from the cells. All together, these results demonstrate the primordial role of organic polymers in iron biomineralization and provide first evidence for the existence of a redox gradient around these nonencrusting, Fe-oxidizing bacteria.

Fe(II) can serve as a source of electrons for phylogenetically diverse microorganisms that precipitate iron minerals as products of their metabolism (see, e.g., references 3, 5, 25, and 30). For example, mixotrophic or autotrophic bacteria can couple the oxidation of Fe(II) to the reduction of nitrate in anoxic and neutral-pH environments. With Fe(III) being highly insoluble at neutral pH, this metabolism leads to the formation of poorly to well-crystallized iron minerals (3, 18, 26, 27) that precipitate partly within the cell periplasm for some strains (22). Similar Fe minerals are also synthesized by autotrophic bacteria that perform anoxygenic photosynthesis, using Fe(II) as an electron donor and light as a source of energy for CO_2 fixation (8, 12, 30), according to the equation $HCO_3^- + 4\ Fe^{2+} + 10\ H_2O \leftrightarrows <CH_2O> + 4\ Fe(OH)_3 + 7\ H^+$.

However, the biological mechanisms of iron oxidation in these bacteria and in particular the way they cope with the formation of minerals within their ultrastructures are still not fully understood. Indeed, iron minerals are potentially lethal since their precipitation may alter cellular ultrastructures but also catalyze the production of free radicals (2). Recent genetic studies of the phototrophic, iron-oxidizing bacteria *Rhodobacter* sp. strain SW2 (6) and *Rhodopseudomonas palustris* strain TIE-1 (16) have identified genes (*fox* and *pio* operons, respectively) encoding proteins specific for iron oxidation. Interestingly, Jiao and Newman (16) suggested that one of these proteins could have a periplasmic localization. However, in contrast to what has been observed in some other phototrophic iron oxidizers (25) and in some nitrate-reducing, iron-oxidizing bacteria (22), no iron-mineral precipitation occurs within the periplasm of the purple nonsulfur iron-oxidizing bacterium *Rhodobacter* sp. strain SW2 (3). Similarly to some other anaerobic neutrophilic (22, 25) and microaerobic iron-oxidizing bacteria (5, 10), this strain seems indeed to have the ability to localize iron biomineralization at a distance from the cells, leaving large areas of the cells free of precipitates (17, 25). While it has been shown that the *Gallionella* and *Leptothrix* genera, for example, produce extracellular polymers that facilitate the nucleation of iron minerals outside cells (see, e.g., references 5 and 9), only a little is known about the existence and function of such polymers in anaerobic, neutrophilic iron-oxidizing bacteria and particularly in the phototrophic strain SW2. In the present study, we investigate iron biomineralization by the photoautotrophic iron-oxidizing bacterium *Rhodobacter* sp. strain SW2. We use scanning transmission X-ray microscopy (STXM) to map and identify organic polymers produced by the cells as well as the redox state of iron at the 25-nanometer scale regularly during a 2 week-period. These results demonstrate the primordial role of organic polymers in iron biomineralization and provide the first evidence for the existence of a redox gradient around SW2 cells.

MATERIALS AND METHODS

Bacterial strain and growth conditions. The phototrophic Fe(II)-oxidizing bacterium *Rhodobacter* sp. strain SW2 (30) was cultivated in batch freshwater mineral medium prepared according to the work of Ehrenreich and Widdel (8) and buffered at pH 6.8 with bicarbonate in equilibrium with a N_2-CO_2 (80:20) atmosphere. SW2 was grown in this medium, with Fe(II) as an electron donor. For experiments using Fe(II) as an electron donor, Fe(II) was added as $FeCl_2$ at a total concentration of 10 mM, which led to the precipitation of a white phase

* Corresponding author. Mailing address: IPGP, 140 rue de Lourmel, 75015 Paris, France. Phone: 0033144279832. Fax: 0033144273785. E-mail: miot@impmc.jussieu.fr.

† Supplemental material for this article may be found at http://aem.asm.org/.

▽ Published ahead of print on 10 July 2009.

characterized as vivianite $Fe_3(PO_4)_2$ (22). This vivianite precipitate was removed prior to inoculation by filtration through 0.22-μm Millipore filters in an anoxic glove box [$p(O_2) < 50$ ppm, where $p(O_2)$ is the partial pressure of O_2 in the glove box]. After filtration, the medium contained 4.5 mM dissolved Fe(II) and less than 0.5 mM phosphate. In uninoculated controls, no further precipitation was observed over the time of the experiment. SW2 was inoculated at a 1/100 dilution ratio from a H_2-pregrown or an Fe(II)-pregrown culture in stationary phase. Cultures were incubated at 20°C under permanent illumination. Growth was followed in duplicate experiments (two independent cultures). For STXM analyses, samples of the same culture were collected in an O_2-free glove box [$p(O_2) <$ 50 ppm] at several subsequent time steps (3 h and 4, 7, 11, and 15 days).

Dissolved Fe(II) and Fe(III) measurement. The concentration of dissolved iron was followed over the time courses of the cultures. For that purpose, 200 μl of a culture suspension was sampled with a syringe and filtered through a 0.22-μm Millipore filter in an anoxic glove box. The dissolved Fe(II) content of the filtrate after dilution in 1 M HCl was determined using the ferrozine assay (28). The presence of dissolved Fe(III) was evaluated as the difference between dissolved Fe(II) concentrations after and before reduction with excess hydroxylamine hydrochloride. No measurable dissolved Fe(III) was evidenced in any sample.

Synthesis of model compounds for Fe redox analyses. To determine the Fe oxidation state in the samples by STXM at the Fe $L_{2,3}$-edges, a pure Fe(II) end member and a pure Fe(III) end member are needed, both of which need a structure as close as possible to that of the phases produced by SW2. Pure Fe(II)-vivianite [$Fe_3(PO_4)_2$] obtained after addition of 10 mM Fe(II) to the culture medium was used as the Fe(II) end member. Nano-goethite (α-FeOOH) obtained from the SW2 culture after 15 days of incubation was used as the Fe(III) end member. The mineralogical purity of these compounds was checked by X-ray diffraction (XRD), and the redox state of Fe in both compounds was also controlled by bulk X-ray absorption near-edge spectroscopy (XANES) at the Fe K-edge. Both reference minerals were rinsed twice with degassed distilled water and dried under vacuum inside an anoxic glove box.

Mineral characterization by XRD. The bulk mineralogical composition of the solid phases formed in SW2 cultures was determined by XRD measurement and compared to those of vivianite and goethite model compounds. Samples were prepared under anoxic conditions in an anoxic glove box. The cultures were centrifuged (5,000 × *g*, 10 min). The solid phases were rinsed twice using degassed distilled water and vacuum dried. The powders were ground in an agate mortar and dispensed in borosilicate capillaries that were sealed with glue before analysis in the diffractometer. This preparation guaranteed strict anoxic conditions for XRD analyses. XRD measurements were performed with Co*K*α radiation on a Panalytical X'Pert Pro MPD diffractometer mounted in the Debye-Scherrer configuration using an elliptical mirror to obtain a high-flux parallel incident beam and an X'Celerator detector to collect the diffracted beam. Data were recorded in the continuous-scan mode within the 5- to 80-degree 2θ range with a step of 0.03 degrees and a counting time of 12 to 24 h per sample.

Scanning electron microscopy. Twenty-eight-day-old samples were chemically fixed using a half-strength Karnovsky solution (20); placed on holey, carbon-coated, electron microscopy copper grids; dehydrated in subsequent steps with an increasing concentration of isopropanol; and finally dried in a Bal-Tec CPD030 critical point dryer. A detailed description of the sample preparation steps is given by Schaedler et al. (24). Dried samples were mounted on aluminum stubs using double-sided carbon tape. For enhanced electrical conductivity, the edges of the electron microscopy grids were painted with conductive silver paste. Samples that showed strong surface charging were coated in a Bal-Tec SCD 40 sputter coater (Bal-Tec, Balzers, Liechtenstein) with a thin layer of Au-Pd (90%-10%, wt/wt). The coating thickness was approximately 20 nm, as determined in focused ion beam cross sections and by a surface texture analyzer (results not shown).

Imaging was performed with a Zeiss Gemini 1550VP field emission scanning electron microscope (SEM) and a Zeiss Gemini 1540XB focused ion beam/field emission SEM. Both microscopes were equipped with Everhart-Thornley secondary electron detectors and in-lens detectors and were optimized to a lens aperture of 30 μm. Images were recorded in a format of 1,024 by 768 pixels at integration times between 15 μs and 45 μs per pixel.

STXM. The samples were constantly kept under an anoxic atmosphere from preparation to transfer and analysis within the STXM microscope, according to the method described in detail in Miot et al. (22). The entire preparation was performed on samples of the SW2 cultures (or of reference compounds) collected at different stages of the culture (3 h to 15 days). STXM experiments were performed on two independent cultures, and two images at least were analyzed for each time point.

Some of the STXM observations at the Fe $L_{2,3}$-edges were performed at Swiss Light Source (SLS; Villigen, Switzerland) on the PolLuX beamline. Some of the observations at the Fe $L_{2,3}$-edges and all the observations at the C K-edge were performed at the spectromicroscopy 10ID-1 beamline at Canadian Light Source (CLS; Saskatoon, Canada). Additional information on the PolLuX beamline can be found in the work of Bernard et al. (4). The 10ID-1 beamline at CLS was described in detail by Kaznatcheev (19). The energy scales for this study were calibrated using the well-resolved 3p Rydberg peak of gaseous CO_2 for the C K-edge and the major peak of hematite at 708.7 eV for the Fe L_3-edge.

Image sequences (stacks) were acquired across the C K-edge and the Fe $L_{2,3}$-edges. as described by Miot et al. (22). No significant beam damage could be observed for typical dwell times used during analyses of the samples (i.e., around 0.8 ms per energy and image point). The aXis2000 software package (15) was used for processing image stacks and XANES spectra according to the procedure described by Miot et al. (22). Normalized Fe $L_{2,3}$-edge XANES spectra of selected regions were fitted with linear combinations of the normalized reference spectra of the Fe(II)-phosphate and goethite model compounds. Standard deviations were calculated from the deviation between the fit and the data and were systematically less than 1%. Fe(III)/total Fe ratio profiles were obtained using the Fe(III) and Fe(II) optical density (OD) maps derived from the stack fits (see Fig. S3 in the supplemental material).

Spectra of reference albumin (protein), xanthan (polysaccharide), and 1,2-dipalmitoyl-sn-glycero-3-phosphocholine (lipid) (7) were recorded at the C K-edge. All these spectra were normalized to an OD corresponding to a 1-nm layer of the compound. Therefore, the measured reference spectra were scaled to match the absorption in the pre- and postedge regions predicted from the elemental composition, densities, and tabulated atomic scattering factors (13). Model spectra were set to an absolute linear absorbance scale (OD per nm of thickness). Spectra recorded at the Fe $L_{2,3}$-edges were normalized as described before. Using aligned stacks recorded at the C K-edge and at the Fe $L_{2,3}$-edges on the same area as well as the normalized reference spectra, we calculated C and Fe speciation maps by singular-value decomposition using the stack fit routine in aXis2000. The algorithm fits the spectra of each individual pixel with a linear combination of the normalized reference spectra plus a constant, accounting for the absorption background of all elements absorbing at lower X-ray energies. We subsequently obtained numbers that were proportional to the amount of organic carbon and to the amount of Fe(III) (though with a different proportion constant) for each pixel of this area. Both series of values were then used to plot the amount of C (polysaccharides on fibers or proteins on cells) relatively to the amount of Fe [Fe(III)] for each pixel of the area (~2,500 pixels in total) and assess the existence of possible correlations (see reference 29 for additional explanations).

RESULTS

Association of iron minerals with organic carbon. Fe(II) was almost completely consumed (oxidized) within 10 days in cultures of SW2 (see Fig. S1 in the supplemental material). In contrast, no significant oxidation could be detected in abiotic controls over the same period. Consistently with the results obtained by Kappler and Newman (17), XRD analyses indicate that the end product of iron oxidation by SW2 is crystalline and consists of nanocrystalline goethite (α-FeOOH) (see Fig. S2 in the supplemental material).

Cell-mineral assemblages were imaged by SEM (Fig. 1a). In addition, iron-rich minerals were localized with respect to the cells by analyzing the cultures using STXM at the Fe $L_{2,3}$-edges. Maps of Fe(II) and Fe(III) were obtained by fitting stacks with a linear combination of Fe(II) and Fe(III) reference compounds. As shown in Fig. 1a and e, iron-rich minerals are exclusively localized outside the cells, mostly on extracellular fibers and in a very low proportion at the cell surface. Extracellular fibers are usually attached to the cell and measure up to a few μm in length and a few nm in diameter (Fig. 1a). Moreover, maps of organic carbon reveal that these iron-bearing fibers are rich in organic carbon (Fig. 1c and d). XANES spectra at the C K-edge obtained for these regions

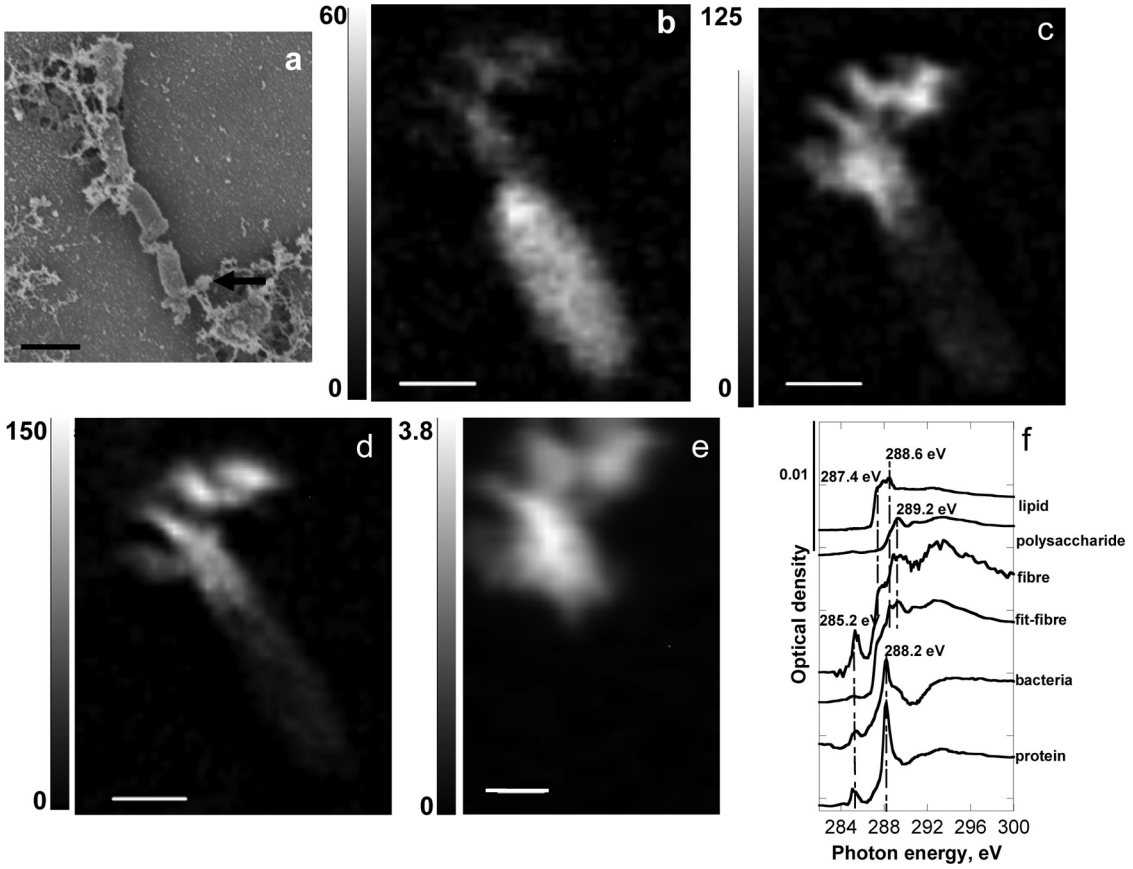

FIG. 1. (a) SEM micrograph showing mineralized fibers (arrow) emerging from SW2 cells. Minerals are located mostly on the fibers, and the surface of SW2 cells remains largely free of precipitates. Scale bar, 1 μm. (b, c, d, e, and f) STXM analyses of a single SW2 cell with mineralized fibers (3-day-old culture). The three different organic carbon maps (b, c, and d) were obtained by fitting an energy sequence of images (stack) with a linear combination of albumin (protein), 1,2-dipalmitoyl-sn-glycero-3-phosphocholine (lipid-fatty acid), and xanthan (polysaccharide). Scale bars, 500 nm. (b) Map of proteins. The cell is clearly visible on this map. (c) Map of lipids. The extracellular fiber is clearly visible on this map. (d) Map of polysaccharides. (e) Fe(III) (goethite) map derived from the stack at the Fe $L_{2,3}$-edges. (f) XANES spectra at the C K-edge obtained on the cell (bacteria) and the extracellular fiber (fibre), compared with the spectra of reference protein, lipid, and polysaccharide. The XANES spectrum of the fiber was fitted with a linear combination of the lipid and the polysaccharide (fit-fibre) and yielded proportions of 50% each.

exhibit maxima of absorption at 285.2 eV, 287.4 eV, and 288.6 eV, which can be attributed to alkene (C═C), aliphatic (C—C) or carbonyl (C═O), and carboxylic (COOH) groups, respectively (Fig. 1f) (14). The biochemical indexation of such spectra is more difficult, given the significant variations of the XANES signatures within some biochemical groups, such as lipids and polysaccharides (A. P. Hitchcock, personal communication). However, the XANES spectrum of the fibers can reasonably well be fitted using a linear combination of a polysaccharide (xanthan) and a fully saturated lipid (1,2-dipalmitoyl-sn-glycero-3-phosphocholine). The peak at 285.2 eV that is not well fitted in intensity with our set of reference spectra can be attributed to additional unsaturated C═C bonds that may be present on the aliphatic tail of the fatty acid. Thus, our results suggest that organic fibers attached to SW2 cells consist of a mixture of partially unsaturated lipids and polysaccharides or of lipopolysaccharides. A maximum of 3% of the total mass of carbon may be accounted for by proteins in these fibers. In contrast, XANES spectra at the C K-edge obtained on bacteria have a dominant absorption maximum at 288.2 eV that is unambiguously attributed to the absorption by the peptidic bond, characteristic of proteins.

The existence of a correlation between the Fe and organic carbon contents on cells and on extracellular mineralized fibers has been investigated separately (Fig. 2) by plotting the OD levels measured on each pixel of the region of interest on the Fe(III) map and on the organic carbon map. Interestingly, the Fe(III) and organic carbon contents are correlated on the mineralized fibers (Fig. 2a) according to a linear relation, $[Fe] = 2.5\,[C] + 100$ ($r = 0.98$). This relation suggests that the amount of Fe(III) precipitated is proportional to the amount of organic carbon on the same area.

The Fe content is also related to the amount of organic carbon on the cells according to a linear relation, $[Fe] = 0.1\,[C] + 25$ ($r = 0.62$). It can be noted that the concentration of iron on the cells is, however, much lower than on the fibers (Fig. 2b), which might correspond to Fe adsorbed to the cells.

Iron oxidation state at the nanoscale. The evolution of the iron redox state in these extracellular iron-rich minerals was followed regularly during a 2-week period (3 h to 15 days of

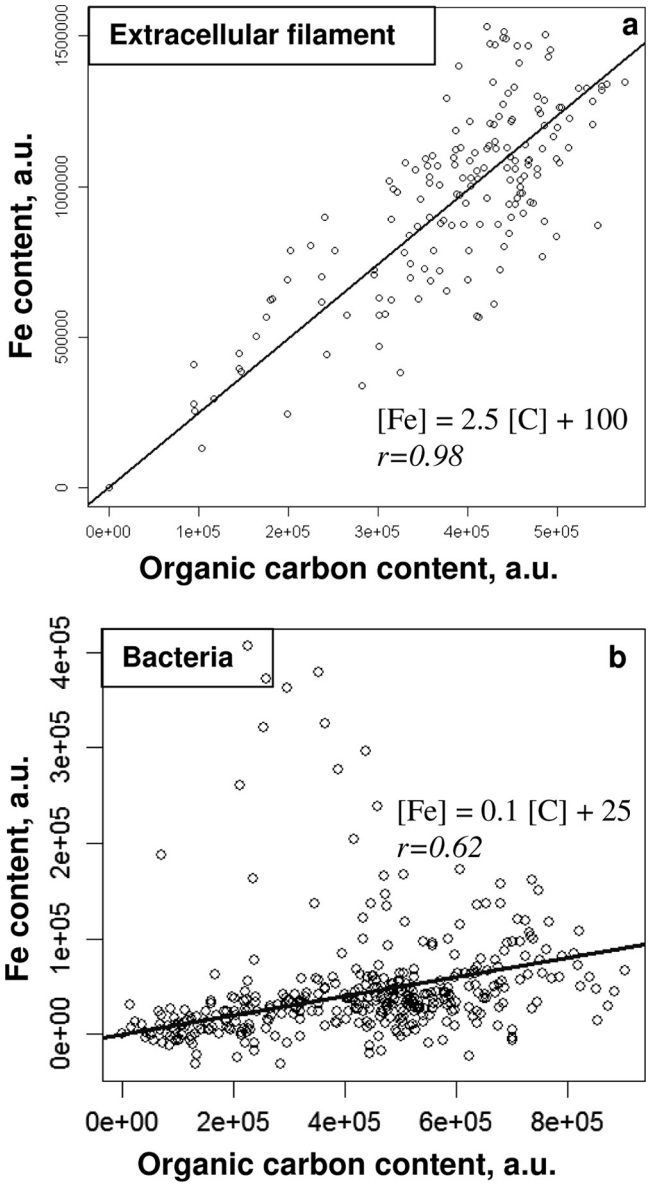

FIG. 2. Correlation analysis of iron contents versus organic carbon contents on extracellular fibers (a) and bacteria (b) from a 3-day-old SW2 culture. Fe and organic carbon contents were estimated at each pixel of the STXM image presented in Fig. 1b to e from the Fe(III), the polysaccharide (for the extracellular fibers), and the protein (for the cell) maps. These results indicate that Fe(III) content is proportional to organic carbon content on extracellular fibers (a) and that cells are covered by a small amount of Fe (b). a.u., arbitrary units.

culture) using STXM at the Fe $L_{2,3}$-edges. XANES spectra recorded on these samples were fit with a linear combination of a reference Fe(II) compound (vivianite) and a reference Fe(III) compound (goethite) (see Fig. S4 in the supplemental material; Table 1). Numerical results of these fits indicate that the minerals that form initially in SW2 cultures are composed of mixed-valence iron [the Fe(III)/total Fe ratio was 0.39 after 3 h of culture]. Over time, iron contained in these minerals becomes increasingly oxidized (see Fig. S3 and S4 in the supplemental material; Table 1). After 7 days of culture, iron-rich minerals are mostly composed of Fe(III) [Fe(III)/total Fe = 0.84], and the end product of iron bio-oxidation by SW2 is a pure Fe(III) compound (nano-goethite obtained after 15 days) (see Fig. S2 in the supplemental material).

Local heterogeneities of the redox state of Fe were investigated at different stages of the culture (Fig. 3). Therefore, Fe(II), Fe(III), and total Fe intensity profiles were derived from Fe(II) and Fe(III) OD maps of the bacteria and associated extracellular iron-rich minerals. The resulting Fe(III)/total Fe profiles along the mineralized fibers from the bacterial pole (pole A) toward the end of the fiber at distance of the cell (pole B) are displayed in Fig. 3b at different time points (5 h and 11 days). This analysis reveals a gradient of the Fe oxidation state along the mineralized fibers [Fe(III)/total Fe = $0.67 - 0.26x$ ($r = 0.88$) (in the 5-h-old sample)] (Fig. 3b), iron being systematically more oxidized at the cell contact than at a distance from the cells. This gradient was observed at all sampling times, and the average iron oxidation state on the filaments increased over time (see Fig. S4 in the supplemental material; Table 1). Toward the end of the experiment, when iron was almost completely oxidized, the redox gradient was attenuated (11 days) [Fe(III)/total Fe = $0.98 - 0.10x$ ($r = 0.82$) (in the 11-day-old sample)] (Fig. 3b).

DISCUSSION

Lipopolysaccharidic fibers act as a template for iron biomineralization. Iron biomineralization by the phototrophic SW2 strain occurs outside the cells (17, 25). The resulting Fe minerals are located mostly on extracellular fibers and partly as patches at the cell surface, but large areas are left uncovered (Fig. 1). This pattern of extracellular iron mineralization differs from that produced by the anaerobic nitrate-reducing BoFeN1 strain, cultured in the same medium, but that was shown to mineralize iron within its periplasm (22, 25). In SW2 cultures, extracellular fibers emerging from the cells (Fig. 1a) show a XANES spectrum at the C K-edge similar to that of a mixture of partly unsaturated lipids and polysaccharides (Fig. 1). Processes of iron oxide particle assembly on organic carbon-containing fibrils have been widely described in the case of iron biomineralization in association with polysaccharides (5, 23). It has been suggested that heterogeneous nucleation of iron oxides at the surface of and within exopolysaccharides proceeds through binding to functional groups (23). Such mechanisms could eventually lead to mineral–organic-compound assem-

TABLE 1. Fe(III)/total Fe quantification obtained from the fit of Fe $L_{2,3}$-edge XANES spectra[a]

Culture time	Mean Fe(III)/total Fe	SD
3 h	0.39	0.006
4 days	0.66	0.005
7 days	0.84	0.005
11 days	0.84	0.004
15 days	1	—[b]

[a] Spectra were extracted from stacks on precipitates collected at different stages of SW2 culture. Fe(III)/total Fe values result from at least two spectrum fits. Standard deviations were calculated as the standard deviations of the fit to the data. SD, means of the standard deviations obtained for each fit.

[b] No standard deviation [reference Fe(III) end member].

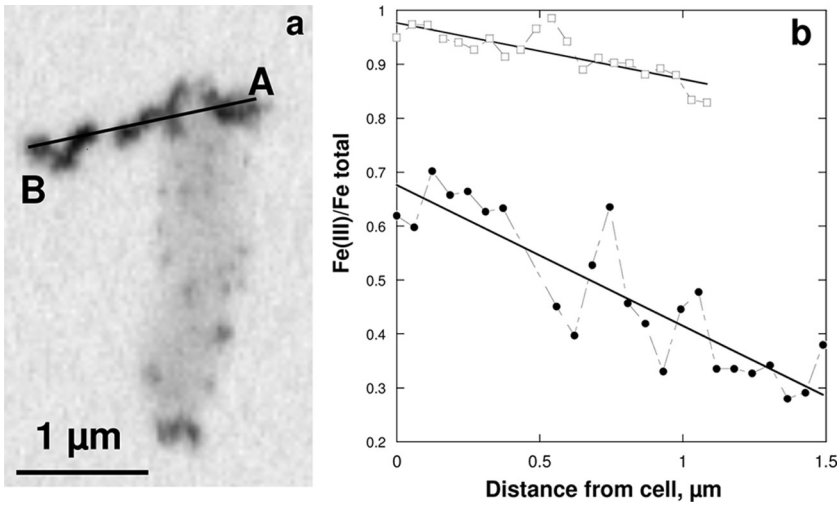

FIG. 3. STXM observations of gradients of the iron oxidation state along mineralized fibers. (a) STXM image (absorption scale) taken at 702 eV (below the Fe L_3-edge) and showing a bacterium and associated extracellular fiber after 5 h. (b) Fe(III)/total Fe ratios along the pole A-pole B profile displayed in panel a (●) and on a fiber from an 11-day-old culture (□) and corresponding linear-curve fits (solid lines). A is the point closest to the pole, and B is the point closest to the tip of the fiber. Fe is more oxidized at the cell contact than at a distance from the cells, and the Fe oxidation state gradient is attenuated with time.

blages with morphologies similar to those evidenced in SW2 cultures. Similar hypotheses can be driven for lipids. Indeed, it has been shown by Archibald and Mann (1) that precipitation of positively charged iron oxides at the surfaces of negatively charged lipid microstructures can lead to tubular organic-inorganic composites (1). In particular, iron oxide (ferrihydrite, magnetite, lepidocrocite, or goethite) precipitation is activated by addition of low levels of sulfated derivatives on galactocerebroside microtubules that serve as a template for mineral assembly (1). These sugar-based lipids exhibit a high negative charge that enhances the binding of cationic Fe(III) species by electrostatic attraction. These binding sites may thus serve as initial foci for mineral nucleation (1). Fibers identified in SW2 cultures may exhibit different types of hydrophilic moieties that could bind Fe(III) (possibly phosphate, sulfate, and hydroxyl groups) and serve as templates for mineral nucleation. This could explain the organic-mineral assemblages of iron oxide nanoparticles clustered at the surface of the organic fibers that are observed in SW2 cultures. This hypothesis is further supported by the linear relationship between Fe and the organic C content on these mineralized fibers (Fig. 2). The following scenario for iron precipitation can thus be proposed. Fe is initially adsorbed onto the fibers proportionally to the amount of organic carbon (acting as binding ligands) present at the surface of the fibers. The linear relationship between Fe and C contents can be preserved after the nucleation step as long as the size of the minerals remains small, as observed in the present study. In contrast, crystal growth would increase the Fe/C ratio, leading in turn to a wide range of Fe concentrations at a given organic carbon concentration. Such a process might account for the presence of a few spots exhibiting a higher Fe content on the cells (Fig. 2b). As shown by Nesterova et al. (23), organic polymers can stabilize very small mineral particles and inhibit further growth.

The organic fibers that act as a template for iron biomineralization in SW2 cultures are elongated appendages (Fig. 1a). XANES spectroscopy suggests that a maximum of 3% in mass of total carbon may be accounted for by proteins in these fibers. In contrast to pili or flagella, which are composed mostly of proteins, fibers observed in SW2 cultures are composed mainly of lipids and polysaccharides. Further analyses will be required to elucidate the origin and the detailed biochemical composition and function of SW2 fibers.

Mineralized fibers exhibit a gradient of Fe oxidation state. The Fe minerals precipitated along the organic fibers record the redox conditions along a section across the microenvironment surrounding SW2 cells. Fe(II) is progressively oxidized to Fe(III), resulting in the formation of nano-goethite in the latest stages (see Fig. S2 in the supplemental material), in agreement with the observations reported by Kappler and Newman (17). As observed by Kappler and Newman (17), at intermediate stages of SW2 cultures (less than 15 days), mixed-valence Fe minerals (see Fig. S4 in the supplemental material; Table 1) might be more amorphous, before transforming into the crystalline end product (nano-goethite) (see Fig. S2 in the supplemental material) (17). In the present study, a gradient of the Fe oxidation state was observed along these organic fibers, with more-oxidized iron minerals in close proximity to the cell and more-reduced iron minerals precipitating at a distance from the cell. Over time, as dissolved Fe(II) becomes completely oxidized, this redox gradient is attenuated and mostly Fe(III) minerals are observed attached to the organic fibers at a distance from the cells. Eventually, the biomineralization process leads to the precipitation of Fe(III)-containing minerals nucleated on the lipopolysaccharidic template. Further biochemical and structural analyses of the fibers produced in SW2 cultures will help in the future in elucidating these mechanisms of iron biomineralization. In particular, additional studies aimed at localizing the sites of iron oxidation, whether it occurs within the periplasm (6, 16), at the cell surface (11, 17, 21), or at the fiber surface, are needed.

ACKNOWLEDGMENTS

We gratefully acknowledge the support of an ANR Jeunes Chercheurs Grant (J.M. and K.B.). CLS is supported by the NSERC, the CIHR, the NRC, and the University of Saskatchewan. The contributions from A.K., F.H., and S.S. were funded by an Emmy-Noether fellowship and, additionally, by the German Research Foundation (DFG) as well as by the University of Tuebingen (Promotionsverbund Bakterien-Material Interaktionen).

We thank Emmanuelle Porcher (MNHN, Paris, France) for correlation analyses. The STXM measurements were performed at CLS, Saskatoon, Canada, and at SLS, Paul Scherrer Institut, Villigen, Switzerland. We thank Konstantine Kaznatcheev, Chithra Karunakaran, and Drew Bertwistle for their expert support of the STXM at CLS. We thank Joerg Raabe and George Tzvetkov for their expert support of the STXM at SLS. We also thank Olivier Beyssac and Sylvain Bernard (ENS, Paris, France) for their help in data collection at SLS. We acknowledge Claus Burkhardt from the NMI Reutlingen for his support in taking the SEM images.

This is IPGP contribution 2536.

REFERENCES

1. **Archibald, D. D., and S. Mann.** 1993. Template mineralization of self-assembled anisotropic lipid microstructures. Nature **364:**430–433.
2. **Auffan, M., W. Achouak, J. Rose, M. A. Roncato, C. Chanéac, D. T. Waite, A. Masion, J. C. Woicik, M. R. Wiesner, and J. Y. Bottero.** 2008. Relation between the redox state of iron-based nanoparticles and their cytotoxicity toward *Escherichia coli*. Environ. Sci. Technol. **42:**6730–6735.
3. **Benz, M., A. Brune, and B. Schink.** 1998. Anaerobic and aerobic oxidation of ferrous iron at neutral pH by chemohetereotrophic nitrate-reducing bacteria. Arch. Microbiol. **169:**159–165.
4. **Bernard, S., K. Benzerara, O. Beyssac, N. Menguy, F. Guyot, G. E. Brown, and B. Goffé.** 2007. Exceptional preservation of fossil plant spores in high-pressure metamorphic rocks. Earth Planet. Sci. Lett. **262:**257–272.
5. **Chan, C. S., G. De Stasio, S. A. Welch, M. Girasole, B. H. Frazer, M. V. Nesterova, S. Fakra, and J. F. Banfield.** 2004. Microbial polysaccharides template assembly of nanocrystal fibers. Science **303:**1656–1658.
6. **Croal, L. R., Y. Jiao, and D. K. Newman.** 2007. The *fox* operon from *Rhodobacter* strain SW2 promotes phototrophic Fe(II) oxidation in *Rhodobacter capsulatus* SB1003. J. Bacteriol. **189:**1774–1782.
7. **Dynes, J. J., T. Tyliszczak, T. Araki, J. R. Lawrence, G. D. Swerhone, G. G. Leppard, and A. P. Hitchcock.** 2006. Quantitative mapping of chlorhexidine in natural river biofilms. Sci. Total Environ. **369:**369–383.
8. **Ehrenreich, A., and F. Widdel.** 1994. Anaerobic oxidation of ferrous iron by purple bacteria, a new-type of phototrophic metabolism. Appl. Environ. Microbiol. **60:**4517–4526.
9. **Emerson, D., and N. P. Revsbech.** 1994. Investigation of an iron-oxidizing microbial mat community located near Aarhus, Denmark: laboratory study. Appl. Environ. Microbiol. **60:**4032–4038.
10. **Hallberg, R., and F. G. Ferris.** 2004. Biomineralization by *Gallionella*. Geomicrobiol. J. **21:**325–330.
11. **Hegler, F., N. R. Posth, J. Jiang, and A. Kappler.** 2008. Physiology of phototrophic iron(II)-oxidizing bacteria—implications for modern and ancient environments. FEMS Microbiol. Ecol. **66:**250–260.
12. **Heising, S., and B. Schink.** 1998. Phototrophic oxidation of ferrous iron by a *Rhodomicrobium vannielii* strain. Microbiology **144:**2263–2269.
13. **Henke, B. L., E. M. Gullikson, and J. C. Davis.** 1993. X-ray interactions—photoabsorption, scattering, transmission, and reflection at E = 50–30,000 eV, Z = 1–92. Atomic Data Nucl. Data Tables **54:**181–342.
14. **Hitchcock, A. P., J. Li, S. R. Reijerkerk, P. Foley, H. D. H. Stöver, and I. Shirley.** 2007. X-ray absorption spectroscopy of polyureas and polyurethanes and their use in characterizing chemical gradients in thin-walled polyurea capsules. J. Electron Spectr. Relat. Phenom. **156–158:**467–471.
15. **Hitchcock, A. P.** 2008. aXis2000—analysis of X-ray images and spectra. A. P. Hitchcock, McMaster University, Hamilton, Canada. http://unicorn.mcmaster.ca/aXis2000.html.
16. **Jiao, Y., and D. K. Newman.** 2007. The *pio* operon is essential for phototrophic Fe(II) oxidation in *Rhodopseudomonas palustris* TIE-1. J. Bacteriol. **189:**1765–1773.
17. **Kappler, A., and D. K. Newman.** 2004. Formation of Fe(III)-minerals by Fe(II)-oxidizing phototrophic bacteria. Geochim. Cosmochim. Acta **68:**1217–1226.
18. **Kappler, A., B. Schink, and D. K. Newman.** 2005. Fe(III) mineral formation and cell encrustation by the nitrate-dependent Fe(II)-oxidizer strain BoFeN1. Geobiology **3:**235–245.
19. **Kaznatcheev, K. V.** 2007. Soft X-ray spectromicroscopy beamline at the CLS: commissioning results. Nucl. Instrum. Methods Phys. Res. A **582:**96–99.
20. **Kiernan, J. A.** 2000. Formaldehyde, formalin, paraformaldehyde and glutaraldehyde: what they are and what they do. Microsc. Today **1:**8–12.
21. **Miot, J., K. Benzerara, G. Morin, S. Bernard, E. Larquet, G. Ona-Nguema, A. Kappler, and F. Guyot.** 2009. Transformation of vivianite by anaerobic iron-oxidizing bacteria. Geobiology **7:**373–384.
22. **Miot, J., K. Benzerara, G. Morin, A. Kappler, S. Bernard, M. Obst, C. Férard, F. Skouri-Panet, J. M. Guigner, N. Posth, M. Galvez, G. E. Borwn, Jr., and F. Guyot.** 2009. Iron biomineralization by neutrophilic iron-oxidizing bacteria. Geochim. Cosmochim. Acta **73:**696–711.
23. **Nesterova, M., J. Moreau, and J. F. Banfield.** 2003. Model biomimetic studies of templated growth and assembly of nanocrystalline FeOOH. Geochim. Cosmochim. Acta **67:**1177–1187.
24. **Schaedler, S., C. Burkhardt, and A. Kappler.** 2008. Evaluation of electron microscopic sample preparation methods and imaging techniques for characterization of cell-mineral aggregates. Geomicrobiol. J. **25:**228–239.
25. **Schaedler, S., C. Burkhardt, F. Hegler, K. L. Straub, J. Miot, K. Benzerara, and A. Kappler.** 2009. Formation of cell-iron-mineral aggregates by phototrophic and nitrate-reducing anaerobic Fe(II)-oxidizing bacteria. Geomicrobiol. J. **26:**93–103.
26. **Straub, K. L., M. Benz, B. Schink, and F. Widdel.** 1996. Anaerobic, nitrate-dependent microbial oxidation of ferrous iron. Appl. Environ. Microbiol. **62:**1458–1460.
27. **Straub, K. L., and B. E. E. Buchholz-Cleven.** 1998. Enumeration and detection of anaerobic ferrous iron-oxidizing, nitrate-reducing bacteria from diverse European sediments. Appl. Environ. Microbiol. **64:**4846–4856.
28. **Viollier, E., P. W. Inglett, K. Hunter, A. N. Roychoudhury, and P. Van Cappellen.** 2000. The ferrozine method revisited: Fe(II)/Fe(III) determination in natural waters. Appl. Geochem. **15:**785–790.
29. **Wan, J., T. Tyliszczak, and T. K. Tokunaga.** 2007. Organic carbon distribution, speciation and elemental correlations within soil micro-aggregates: applications of STXM and NEXAFS spectroscopy. Geochim. Cosmochim. Acta **71:**5439–5449.
30. **Widdel, F., S. Schnell, S. Heising, A. Ehrenreich, B. Assmus, and B. Schink.** 1993. Ferrous iron oxidation by anoxygenic phototrophic bacteria. Nature **362:**834–836.